INTERNATIONAL JOURNAL OF INTEGRATED ENGINEERING
ISSN: 2229-838X e-ISSN: 2600-7916

IJIE

Vol. 17 No. 8 (2025) 341-361
https://publisher.uthm.edu.my/ojs/index.php/ijie

Aerodynamic Analysis of S809 Airfoil: A Stall Validation with RANS k-ω Turbulence Models

Abobakr Al-Ttowi[1], Akmal Nizam Mohammed[2]*

[1] *Faculty of Mechanical and Manufacturing Engineering, Universiti Tun Hussein Onn Malaysia (UTHM), Parit Raja 86400, MALAYSIA*
[2] *Center for Energy and Industrial Environment Studies, Universiti Tun Hussein Onn Malaysia (UTHM), Parit Raja 86400, MALAYSIA*

*Corresponding Author: akmaln@uthm.edu.my
DOI: https://doi.org/10.30880/ijie.2025.17.08.028

Article Info

Received: 1 August 2025
Accepted: 30 November 2025
Available online: 31 December 2025

Keywords

CFD, airfoil, wind turbine, angle of attack, turbulence model

Abstract

This study examines the aerodynamic efficacy of the S809 airfoil at six angles of attack: −14.23°, −5.15°, 0°, 5.13°, 9.22°, and 10.21°. It uses steady two-dimensional RANS with two closures: k–ω SST (Menter) and k–ω Standard. It also checks the results against wind-tunnel data from NREL. We digitized experimental pressure distributions with calibrated axes, which meant that there was a vertical error of ±0.03 in Cp was used, and the uncertainty in the integrated lift is about 10^{-3}. Without re-processing, the reported experimental uncertainties from NREL were kept. The study links coefficient trends to the measured surface-pressure fields so that you don't have to use integrals to see if they agree. Both models have a pre-stall range of 5.13° to 9.22°, and the curves and wake thickness match the measurements. The slope of the lift curve is also very close to what was found. There are differences between the start of the stall and the end of the load. The k–ω SST model gets the order of the stalls right, but it makes them less intense. This means that the lift is a little too high and the pressure drag is a little too low at 9.22° and 10.21°. The k–ω Standard model keeps separation from happening longer and gives the biggest lift overprediction and the lowest drag in the same range. When the incidence is negative, both models predict fewer losses than the tunnel data. The solutions show a small positive lift and drag matches well at about 0°. This means that the problem is with the residual circulation offset and not the friction model. The results show that design and control can work well between 5.13° and 9.22°. They also show where you need to calibrate or control the transition as the separation gets closer. A subsequent study will employ URANS to broaden the scope into the post-stall regime to rectify unsteady phenomena.

1. Introduction

The urgent demand for renewable energy solutions has positioned wind power as a central component of the global transition toward sustainable energy systems. The aerodynamic efficiency of wind turbine blades directly influences energy capture, operational stability, and structural loading. Since turbine blades are constructed from airfoil sections, accurately predicting their aerodynamic behavior across a range of angles of attack (AoA) is critical for blade design and performance optimization [1], [2]. Computational Fluid Dynamics (CFD) has become

an indispensable tool in this regard, enabling detailed flow-field analysis and aerodynamic prediction with reduced experimental cost and greater design flexibility [3].

The NREL S809 airfoil, developed for horizontal-axis wind turbines (HAWTs), is among the most widely investigated geometries for both experimental and numerical research. Its inclusion in the NREL Phase VI rotor and availability of extensive experimental datasets make it a reliable benchmark for CFD validation studies [4], [5]. Consequently, the S809 airfoil has been extensively used in aerodynamic investigations aimed at improving predictive accuracy, assessing turbulence model performance, and identifying optimum operating AoA.

Despite this extensive body of work, numerical simulations of the S809 airfoil continue to exhibit discrepancies with experimental data, particularly at high AoAs and near stall. These deviations are often linked to turbulence model limitations, mesh resolution strategies, and near-wall treatment approaches [6], [7]. For instance, the standard and Shear Stress Transport SST k-ω models are computationally robust. The standard k-ω model improves near-wall resolution but tends to mispredict drag and stall onset. The Shear Stress Transport (SST) k-ω model, designed to overcome the addressed issue, generally performs better for separation and stall prediction, though it has been observed to overpredict lift coefficients in certain regimes [8], [9], [10].

To address these modeling uncertainties, the present study conducts a comprehensive CFD investigation of the S809 airfoil over a range of AoA (−14.23° to +10.21°) at a Reynolds number of 2.0×10^6. Simulations were performed in ANSYS Fluent using a structured mesh and validated through a Grid Convergence Index (GCI) study.

The primary objectives of this study are: (i) To investigate the influence of variable angle of attacks at the aerodynamic performance of the airfoil; (ii) To evaluate the RANS k-w turbulence models aerodynamics performance of the airfoil; and (iii) To validate the overall CFD performance with NREL experimental work. The main contributions are: (a) provision of grid-converged aerodynamic data for S809 at Re = 2.0×10^6; (b) evaluation of turbulence model strengths and limitations in predicting aerodynamic coefficients; and (c) identification of the k-ω SST model as the most reliable for optimum AoA prediction under validated conditions.

Beyond the specific focus of this work, numerous researchers have explored turbulence models in the context of wind turbine aerodynamics. Early investigations established the limitations of the standard k-ε model for separated flows, where its isotropic turbulence assumption leads to premature reattachment and underestimation of drag at high angles of attack [11], [12]. Variants such as the RNG k-ε and realizable k-ε introduced additional correction terms, improving performance in moderate separation flows, though still proving inadequate in deep stall [13],[14]. The k-ω family, with its inherent sensitivity to near-wall gradients, demonstrated improved fidelity in attached flows, but often exaggerated drag forces at moderate to high AoA [9]. The SST k-ω model, which blends k-ω near the wall with k-ε away from it, emerged as a more balanced alternative, capturing separation and stall onset more reliably than either parent [5] model. Nevertheless, overprediction of lift has been consistently observed across multiple studies [8], [15].

Other two-equation models have also been tested on S-series airfoils and turbine blades. The Spalart–Allmaras (SA) model, originally developed for aerospace applications, has been applied in wind energy research due to its computational efficiency and robustness in attached boundary layers [16]. However, for S809-type profiles, SA has generally been reported to underpredict stall severity and misrepresent wake structures [17]. The Reynolds Stress Model (RSM), which resolves the transport of Reynolds stresses rather than relying on isotropic eddy viscosity assumptions, demonstrated improved accuracy in highly separated flows but at significantly higher computational cost [18]. Hybrid methods such as Detached Eddy Simulation (DES) and hybrid RANS–LES approaches have also been explored, offering improved resolution of unsteady separation and vortex shedding phenomena [19]. Large-Eddy Simulation (LES), while computationally prohibitive for full turbine modeling, has been successfully used in academic studies of S809 and other wind turbine sections to capture transitional stall and wake turbulence with high fidelity [20].

Comparative studies have highlighted both the promise and the challenges of these models. Zhong [8] demonstrated that calibrated SST formulations improved stall prediction for wind turbine airfoils, while Younoussi et al. [15] developed a model calibration strategy for stall-dominated flows that significantly enhanced accuracy without prohibitive computational cost. At the rotor level, Sørensen and Shen [6] showed that turbulence model choice strongly influences wake predictions, with implications for turbine spacing and farm design. Recent optimization frameworks, such as those presented by Akram et al. [1] and Dhert et al. [2], have coupled RANS-based CFD with adjoint optimization, underscoring that turbulence model fidelity directly affects the accuracy of design-driven aerodynamic improvements.

In summary, the literature consistently indicates that turbulence modeling remains the dominant source of uncertainty in CFD predictions for wind turbine airfoils. While k-ε, k-ω, and SST k-ω remain the most widely applied two-equation closures, alternatives such as SA, RSM, DES, and LES have each offered incremental improvements at the expense of complexity or computational resources. This body of research establishes a critical context for the present study, which contributes by systematically evaluating two widely used RANS turbulence models of k-ω under grid-independent conditions for the S809 airfoil, while explicitly identifying the optimum AoA and clarifying turbulence-model suitability for predictive aerodynamic analysis.

Int. Journal of Integrated Engineering Vol. 17 No. 8 (2025) p. 341-361

Nomenclature		
CFD	Computational fluid dynamics	-
NREL	National Renewable Energy Laboratory	-
LES	Large eddy simulation	-
Re	Reynolds number	-
V	Free stream velocity	m/s
L	Characteristic length	m
μ	Dynamic viscosity	kg/ms
u_τ	Friction velocity	m/s
Δy	Distance from the wall to the center of the first computational cell	m
ν	Kinematic viscosity of the fluid	m^2/s
k	Turbulence kinetic energy	m^2/s^2
ε	Turbulence dissipation rate	m^2/s^3
ω	Specific dissipation rate	1/s
U	Wind velocity at distance x	m/s
U_0	Free-stream wind velocity	m/s
D	Rotor diameter	m
ρ	Air density	kg/m^3
μ	Dynamic viscosity	Pa·s
μ_T	Eddy viscosity	Pa·s
σ	Closure coefficient	-
τ	Reynolds stress tensor	Pa
Y+	Wall distance	-
k-epsilon	Standard k-ε turbulence model	-
k-ω	Standard k-ω turbulence model	-
k-ω SST	Shear stress transport k-ω turbulence model	-
T	Torque	N·m
Cp	Pressure coefficient	-
Cd	Drag coefficient	
Cl	Lift coefficient	
α\alphaα	Closure coefficient for turbulence models	-
Ø	Flow angle or the angle of attack	Degrees/Rad
LE	Leading edge	-
TE	Trailing edge	-

2. Materials and Methods

In the numerical simulations, ANSYS Fluent was used to solve the RANS mass and momentum equations. In order to solve the mass and momentum equations with stability, accuracy, and computing efficiency, the aerodynamic performance of the S809 airfoil was simulated using ANSYS Fluent to solve the steady, incompressible Reynolds-Averaged Navier–Stokes (RANS) equations. The analysis was conducted in two dimensions with air as the working fluid, having a density of 1.225 kg/m^3 and a dynamic viscosity of 1.802×10^{-5} kg/m·s. A pressure-based solver with SIMPLE pressure–velocity coupling was used, and all transport equations were discretized using a second-order upwind scheme. Convergence was achieved when the scaled residuals reached 10^{-5} and the lift and drag coefficients stabilized as well as other residuals as shown in Figure 1, Figure 2, and Figure 3.

The ANSYS Fluent Theory Guide [21] states that fully resolving the viscous sublayer with $y^+ \lesssim 1$ is necessary for wall-resolved k-ω type models. Near-wall modelling used wall-resolved k–ω equations integrated to the wall. The first cell height gave y+ ≈ 0.49 (max 0.68, min 0.012), fully resolving the viscous sublayer; No wall functions were used; the near-wall mesh resolves the viscous sublayer. Based on the grid spacing of the near wall cell, (Δs) was obtained from Pointwise CFD online tool and determined by $\Delta s = 1.2367 \times 10^{-5}$ m. Notably, since $\Delta y = 6.4722 \times 10^{-6}\text{m} < \Delta s = 1.2367 \times 10^{-5}$ m; the mesh is assumed to be good enough to capture the boundary layer. Post-simulation analysis confirmed this satisfied the y+<1 criterion, as shown in Figure 4. The resulting y+

values, the maximum y+ of 0.684137 occurs at the leading edge where x/c = 0.000199023, while the minimum y+ 0.0115865 is found near the trailing edge where x/c = 0.990737.

$$Re = \frac{\rho \times V \times L}{\mu} \quad (1)$$

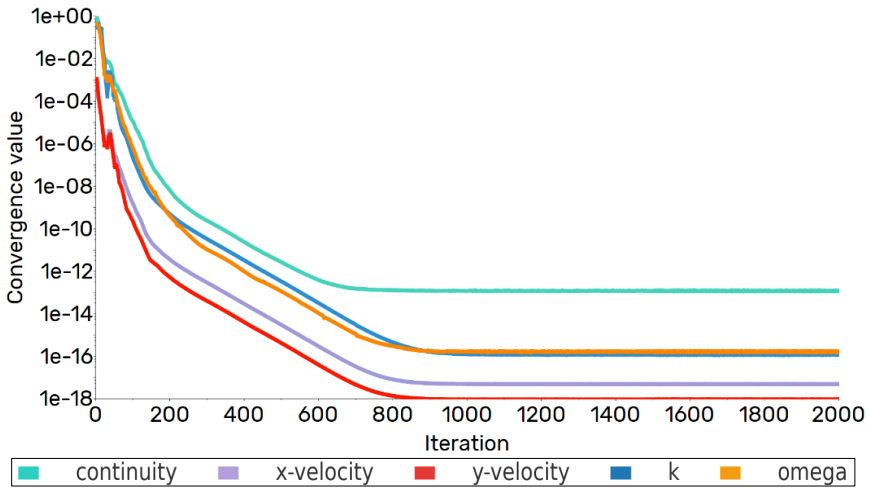

Fig. 1 *Scaled residual and convergence*

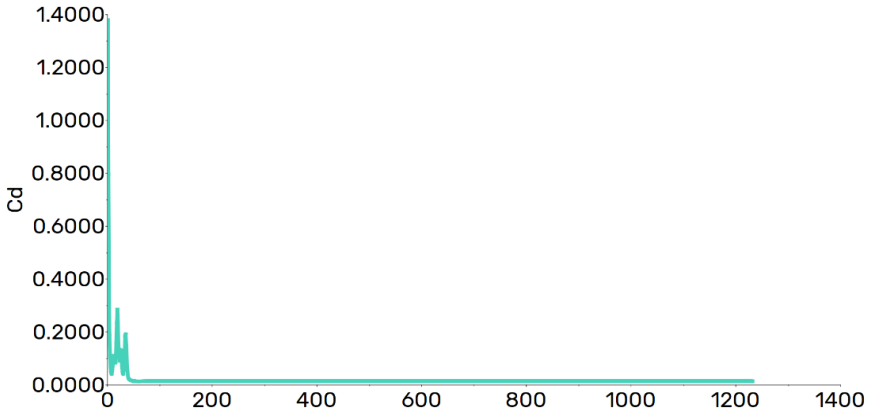

Fig. 2 *Cd convergence*

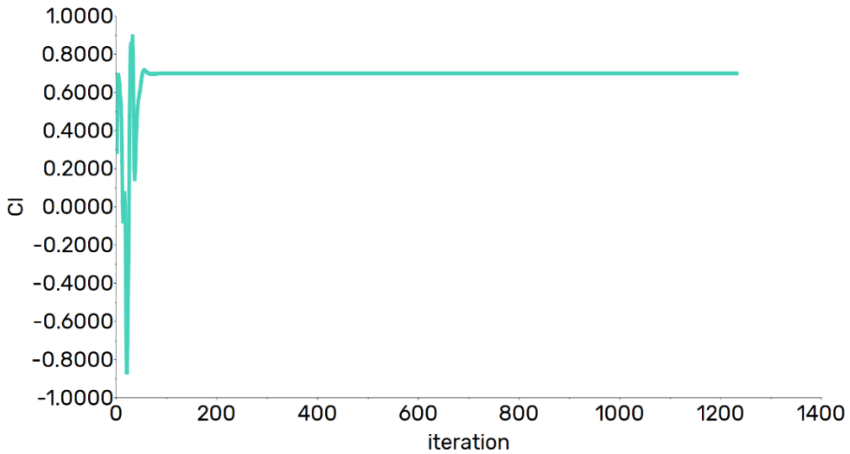

Fig. 3 *Cl convergence*

Int. Journal of Integrated Engineering Vol. 17 No. 8 (2025) p. 341-361

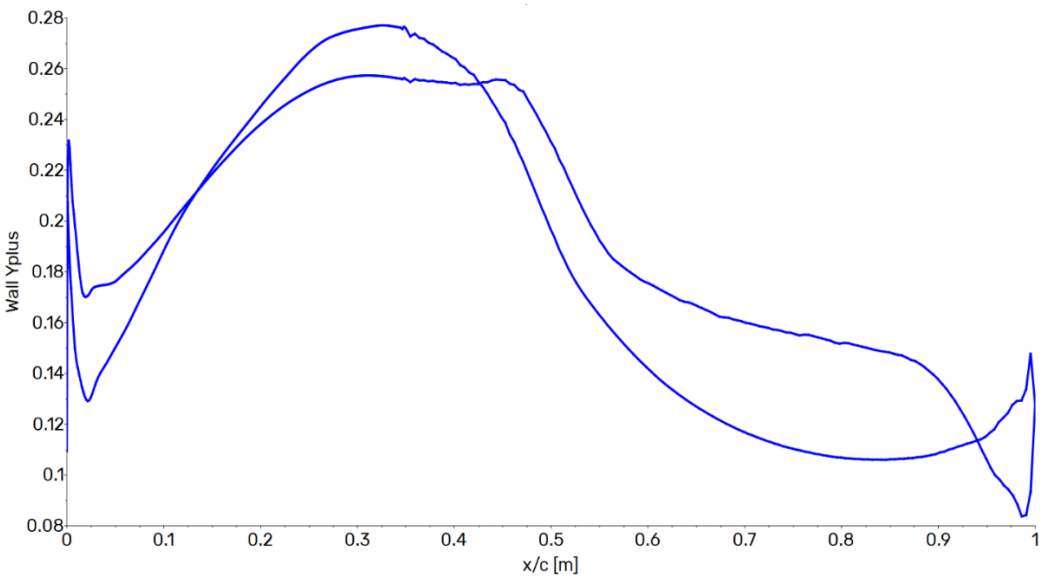

Fig. 4 *y+ distribution along the chord length (x/c) of the S809 airfoil*

The external 2-D domain extended 7.5 c from the airfoil in all directions (15 c total diameter). The left boundary was a velocity-inlet with free-stream speed U= 29.42 m/s applied along the prescribed AoA. Inlet turbulence was specified by Intensity and Viscosity Ratio with I = 0.5% and μt/μ = 0.07. The right boundary was a pressure-outlet at 0 Pa gauge; backflow turbulence used the inlet settings. The upper and lower outer boundaries, located 7.5c from the airfoil, were sufficiently distant to yield negligible gradients and thus represent free-stream conditions. A steady, pressure-based RANS solver was used (2-D planar, absolute velocity formulation) with Coupled pressure–velocity coupling. Least-Squares Cell-Based gradients were used; Second-Order pressure and Second-Order Upwind schemes were applied for momentum, k, and ω. Default under-relaxation factors were retained. Convergence was declared when normalized residuals < $10^{-5}$and lift and drag and residual monitors reached steady. The study used k-ω standard and k-ω SST (Menter) as implemented in Fluent. For the SST runs, Production Limiter was enabled; default model constants were used.

NREL S809 airfoil shown in Figure 5 is an airfoil that is used as a geometry in the NREL phase VI is two bladed turbine with 10.058 diameter (Radius = 5.029 m) and has been chosen in this study for an easy validated comparison. The airfoil geometry coordinates were obtained from [22] which is an airfoil specialized website. The leading edge, trailing edge, upper surface or suction side, and lower surface or pressure side are the four distinct parts of a typical airfoil. The connecting line or the chord line is defined the line connecting both the leading edge and a trailing edge. Mean camber line is the curve that runs through the centre of an airfoil's upper surface and lower surfaces. In Figure 6, the standard airfoil structure is pictured. The completed figure with all meshing and boundary conditions is illustrated in Figure 7. While the domain is shown in Figure 8. Blockage/tunnel correction. The domain height is 15 c and the S809 maximum thickness is ≈0.21 c [23], giving a blockage ratio $t/H \approx 0.21/15 \approx 1.4\%$. Because this is < 5%, no wind-tunnel wall/blockage correction was applied.

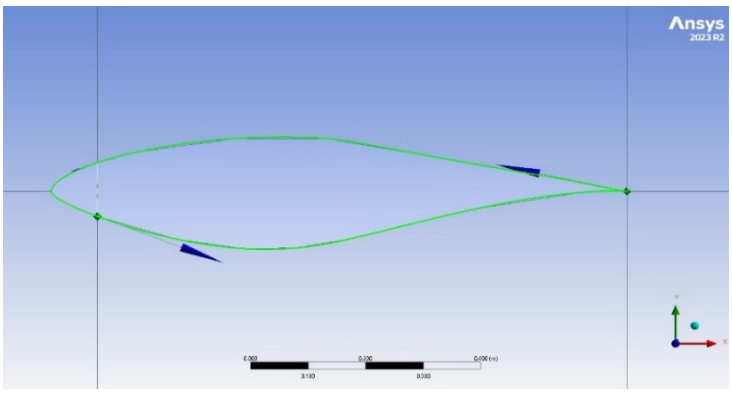

Fig. 5 *NREL S809 airfoil in ANSYS design modeler*

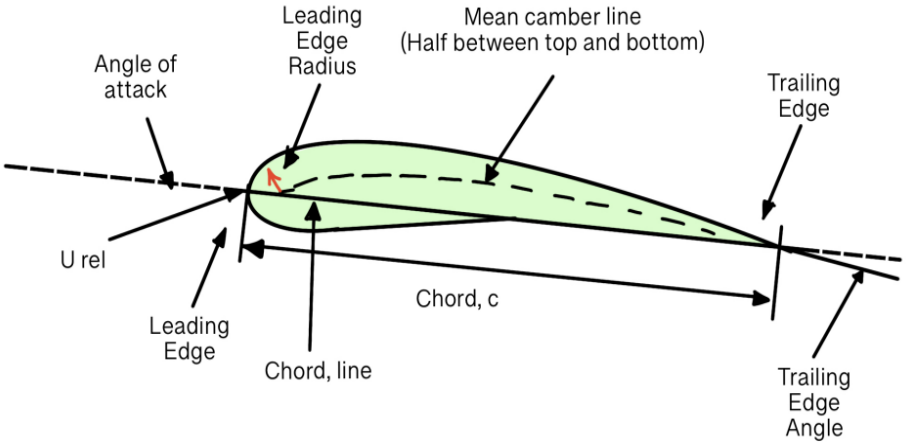

Fig. 6 *Typical airfoil parameters*

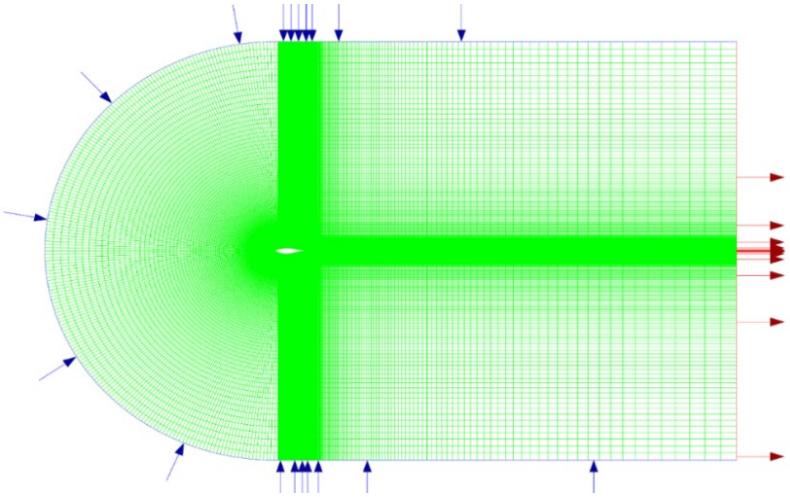

Fig. 7 *S809 airfoil completed meshing and boundary conditions*

Table 1 *List of NREL S809 airfoil considered parameters*

Input parameter	Magnitude	Input parameter	Magnitude
Angle of attack	variable	Density of Fluid	$1.225\ \frac{\text{kg}}{\text{m}^3}$
Kinematic viscosity	1.802×10^{-5}	Turbulence model	variable
Iterations Numbers	2000	Operating Pressure	0 gauge (1atm)
Solution method	Second order upwind	Operating Temperature	15 C
Length	1 m	Velocity flow	29.42 m/s
Solver type	Pressure-based	Time	Steady
Re	2.0×10^6	Convergence	Exact residual and force history stability

Int. Journal of Integrated Engineering Vol. 17 No. 8 (2025) p. 341-361

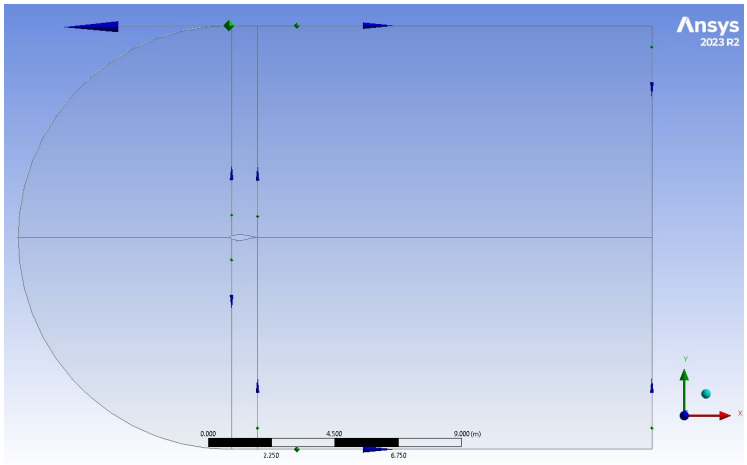

Fig. 8 *S809 airfoil numerical study domain*

2.1 Mesh

Based on Richardson Extrapolation, the characteristic cell size was defined which is in this case a 2D using the equation shown below Where A_i/V_I is the area/volume of the ith cell, N is the number of cells. After that, create 3 meshes of size h_1, h_2, h_3 (where $h_1 < h_2 < h_3$ i.e. fine =1, medium =2, coarse = 3) with a refinement factor r > 1.3 Where $r_{21} = \frac{h_2}{h_1}$, $r_{32} = \frac{h_3}{h_2}$. E.g. from the 2D case, to reduce element size of 2mm by $\sqrt{2}$, refinement factor would be $r = \frac{2mm}{\frac{2mm}{\sqrt{2}}} = \sqrt{2} = 1.414 > 1.3$. Thus, reducing element size by root 2 in 2D (and thus doubling element count) meets criteria. (For 3D $r = \frac{2mm}{\frac{2mm}{\sqrt[3]{2}}} = \sqrt[3]{2} = 1.26 \approx 1.3$, just about meets criteria). Third, calculate apparent order of accuracy, p (for a constant refinement factor r) using equation 2 Where $\epsilon_{32} = \phi_3 - \phi_2, \epsilon_{21} = \phi_2 - \phi_1$. With that being done, calculate extrapolated values (value if cell size approaches 0) would be the fourth step using equation 4. The type of convergence is decided based on $\frac{\epsilon_{21}}{\epsilon_{32}}$ as per the following four cases:

- $0 < \frac{\epsilon_{21}}{\epsilon_{32}} < 1$; Monotonic convergence
- $-1 < \frac{\epsilon_{21}}{\epsilon_{32}} < 0$; Oscillatory convergence
- $s\frac{\epsilon_{21}}{\epsilon_{32}} < -1$; Oscillatory Divergence
- $\frac{\epsilon_{21}}{\epsilon_{32}} > 1$; Monotonic Divergence

$$h = \left[\frac{1}{N}\sum_{i=1}^{N} A_i\right]^{\frac{1}{2}} \tag{2}$$

$$p = \frac{1}{ln\,(r)} \left| ln\left(\frac{\epsilon_{32}}{\epsilon_{21}}\right)\right| \tag{3}$$

$$\phi_{ext}^{21} = (r^p\phi_1 - \phi_2)/(r^p) \tag{4}$$

To ensure the reliability of the simulation results, a single-variable mesh independence study was conducted using structured mesh configurations with systematically refined edge divisions. Three mesh densities were evaluated: coarse, medium, and fine, with total element counts of 119,992, 240,950, and 479,120, respectively as shown in Table 2. The refinement strategy focused on increasing the number of divisions across key edge regions influencing flow characteristics, including the leading and trailing edges. The mesh was prepared in ANSYS Meshing. Global controls used no adaptive sizing and a growth rate of 1.2; mesh defeaturing was enabled with a defeature size of 6.764×10^{-3}m. Curvature capture was enabled with a curvature minimum size of 1.3521×10^{-2}m, proximity capture was off. The model reports a bounding-box diagonal of 27.042 m, average surface area 52.169 m^2, and minimum edge length 2.2216×10^{-7} m. Mesh quality checks were on with Medium smoothing. Boundary-layer inflation used Smooth Transition with transition ratio 0.272, 2 layers, growth rate 1.2, and the Pre algorithm. Four local edge sizing were applied: (1) 7 edges with 424 divisions, behavior Soft, bias factor 40 000 with reverse bias on 4 edges; (2) 3 edges with 212 divisions, behavior Hard, bias factor 300 with reverse bias on 2 edges; (3) 4 edges with 141 divisions, behavior Hard, no bias; and (4) 4 edges with 212 divisions, behavior Hard, no bias. These settings concentrate nodes near key boundaries while keeping orderly growth into the far field.

Mesh quality was consistent across the three grids (M1–M3) while resolution increased from 119,992 to 240,000 to 479,120 elements (nodes 120,664 to 240,950 to 480,462). The average skewness remained low and essentially

unchanged (0.1056 to 0.1050 to 0.1045), and the maximum skewness decreased slightly (0.5909 to 0.5896 to 0.5886); both values fell well within excellent limits (0-0.25) and (0.95-1.00) for skewness and orthogonal quality, respectively. The average orthogonal quality was high on all grids (0.9538 to 0.9561 to 0.9577), with the maximum equal to 1.00 for each case. Importantly, the minimum orthogonal quality improved monotonically with refinement (0.281 to 0.338 to 0.391), indicating removal of the weakest cells as the mesh was refined. Overall, these metrics place the meshes in the good–excellent range and confirm that refinement did not degrade quality, providing a dependable basis for the grid-sensitivity and validation studies as tabulated in Table 3.

Table 2 *Mesh division details for coarse, medium, and fine grids in single-variable GCI study of S809 airfoil*

Refinement	Edge Sizing 1 (# divisions)	Edge Sizing 2 (# divisions)	Edge sizing 3 (# divisions)	Edge Sizing 4 (# divisions)	# Elements
Coarse	212	106	71	106	119,992
Medium	300	150	100	150	240,950
Fine	424	212	141	212	479,120

Table 3 *Mesh quality study*

Metric	M1 (coarse)	M2 (medium)	M3 (fine)
Number of Elements	119992	240000	479120
Number of Nodes	120664	240950	480,462
Avg skewness	0.10562	0.10497	0.1045
Max skewness	0.59088	0.5896	0.58863
Min skewness	1.3057×10^{-10}	1.3057×10^{-10}	1.3057×10^{-10}
Avg orthogonal quality	0.95382	0.95605	0.95772
Max orthogonal quality	1.00	1.00	1.00
Min orthogonal quality	0.2813	0.33737	0.39091

This systematic refinement aimed to capture detailed boundary layer behaviour and flow separation more accurately, particularly in high-gradient regions. The resulting mesh configurations were used in conjunction with GCI (Grid Convergence Index) analysis to quantitatively assess discretization errors and determine mesh independence. The overall meshing of the airfoil is shown in Figure 9.

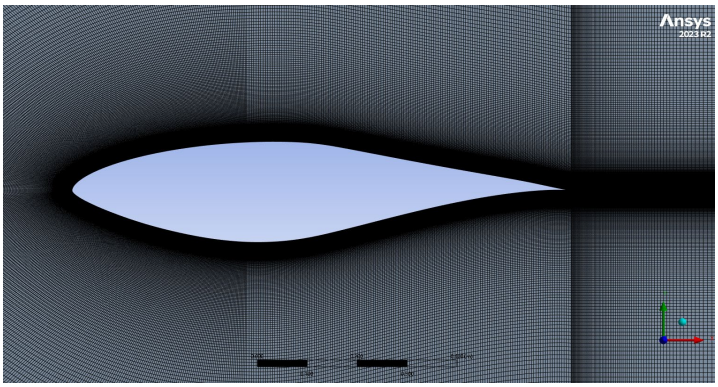

Fig. 9 *S809 airfoil refined mesh*

A grid convergence study was conducted using the Grid Convergence Index (GCI) method to evaluate the sensitivity of the lift and drag coefficients to mesh refinement as tabulated in Table 4 and Table 5. Three systematically refined grids coarse, medium, and fine were used, with refinement ratio r =1.414. The results were analysed for monotonic convergence behaviour, with apparent orders p of 6.660 and 5.374 for the lift and drag coefficients, respectively. The lift coefficient (CL) exhibited monotonic convergence with GCI_{fine21} of 0.035% and a 13.47% underprediction compared to experimental data. Conversely, the drag coefficient (CD) showed

Int. Journal of Integrated Engineering Vol. 17 No. 8 (2025) p. 341-361

monotonic convergence but with a slight overprediction of 16.486%, and a $GCI_{fine\,21}$ of 0.351%. The validation supports mesh independence of the fine mesh, with acceptable error margins for both aerodynamic coefficients.

Table 4 *Grid Convergence Index (GCI) analysis for lift and drag coefficients of the S809 airfoil using single-variable mesh refinement*

Calculations	Experimental data	ANSYS fluent coarse φ3	ANSYS fluent medium φ2	ANSYS fluent fine φ1	ε32	ε21	ε21/ε32	Behavior	p	φext21
CL	1.360	1.143	1.173	1.176	-0.030	-0.003	0.099	Monotonic Convergence	6.660	1.177
CD	0.019	0.024	0.022	0.022	0.002	0.000	0.155	Monotonic Convergence	5.374	0.022

Table 5 *Grid Convergence Index (GCI) analysis for lift and drag coefficients of the s809 airfoil using single-variable mesh refinement (continued)*

φext32	ea21	eext21	GCI fine21	GCI fine21 (%)	% error to exp	decision of error
1.177	0.003	0.000	0.000	0.035	-13.470	Underpredict
0.022	0.015	0.003	0.004	0.351	16.486	Overpredict

Figure 10 presents the pressure coefficient (Cp) distribution comparison between experimental measurements and numerical results for different mesh densities (coarse, medium, and fine). The Cp values are plotted along the normalized chord length (x/c) for both the upper and lower surfaces of the S809 airfoil at the selected angle of attack. Overall, the CFD results exhibit good agreement with the experimental data, particularly in the pressure recovery region near the trailing edge. Notably, finer meshes tend to capture the suction peak and pressure gradients more accurately, especially around the leading edge. Despite minor discrepancies in the lower surface, the variation among the coarse, medium, and fine grid predictions is minimal, reinforcing the reliability of the medium and fine grids for further analysis. This validation confirms the robustness of the mesh refinement and supports the findings from the Grid Convergence Index (GCI) analysis.

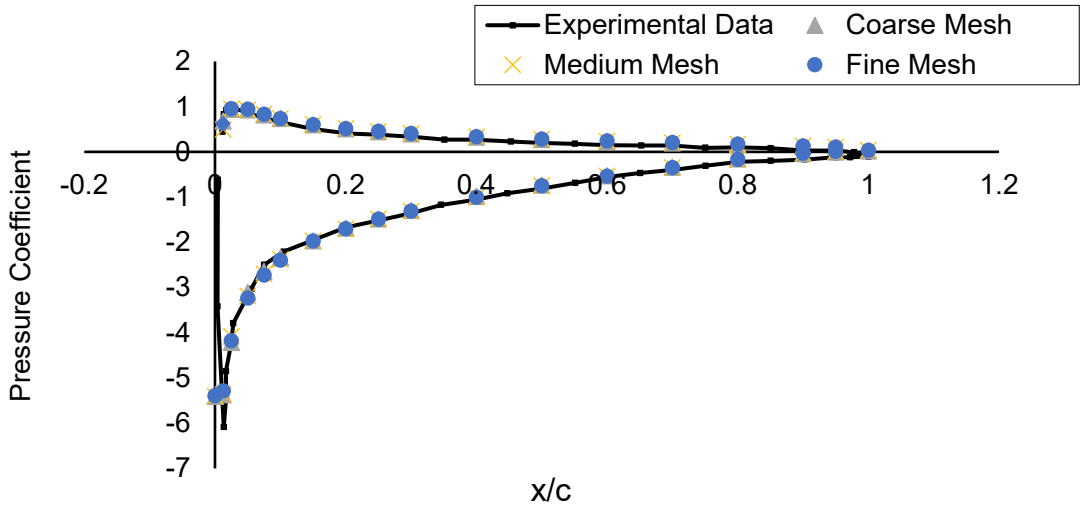

Fig. 10 *pressure coefficient (Cp) distribution comparison between experimental measurements and numerical results for different mesh densities (coarse, medium, and fine)*

2.2 Flow Conditions

The simulations for the S809 airfoil were conducted under standard sea-level atmospheric conditions. The freestream velocity was maintained at 29.42 m/s, producing a Reynolds number of 2.0×10^6 based on a chord length of 1.0 m. The air properties used in the simulations included a density of 1.225 kg/m^3 and a dynamic viscosity of 1.802×10^{-5} kg/m·s, corresponding to a standard temperature of 293 K and pressure of 101,325 Pa.

A series of angles of attack (α) ranging from -14.23° to +10.21° were selected to examine the airfoil's aerodynamic performance. For each angle, the cosine and sine values were calculated to project the lift and drag forces into their respective X and Y directional components. The tabulated values in Table 6 include the coefficients of lift and drag alongside their trigonometric decompositions.

Table 6 *S809 airfoil flow conditions*

α (°)	Re	ρ (kg/m³)	μ (kg/m.s)	L (m)	U (m/s)	cos(α)	sin(α)
-14.23	2.00E+06	1.2250	1.802E-05	1.0000	29.4204	0.9693	-0.2458
-5.14	2.00E+06	1.2250	1.802E-05	1.0000	29.4204	0.9960	-0.0896
0	2.00E+06	1.2250	1.802E-05	1.0000	29.4204	1.0000	0.0000
5.13	2.00E+06	1.2250	1.802E-05	1.0000	29.4204	0.9960	0.0894
9.22	2.00E+06	1.2250	1.802E-05	1.0000	29.4204	0.9871	0.1602
10.21	2.00E+06	1.2250	1.802E-05	1.0000	29.4204	0.9842	0.1773

2.3 Digitization

Reference data for the S809 airfoil shows pressure coefficient distributions with respect to location on the airfoil for each AoA, $C_p(x/c, \alpha)$ and as well as lift and drag coefficients C_L, C_D which were taken from the published NREL S809 wind-tunnel datasets [23]. This plot shows C_p versus x/c for the S809 airfoil at $\alpha = -14.23°, -5.15°, 0°, 5.13°, 9.22°$,and $10.21°$. Curves were digitized from the NREL figures using WebPlotDigitizer (v4.x) after calibrating the axes to x/c $[0,1](m)$and $C_p[-4,1]$. Both parameters were traced separately with dense picking and data were exported to CSV and down sampled for display to keep the figure readable. Vertical error bars are ±0.03 in $C_p$at every x/c. This value was obtained directly from the calibrated image resolution. The original NREL figure [23] used in this work spans $C_p = +1$ to $C_p = -4$, i.e. a total range of 5.0 $C_p$units over 618 pixels in the vertical direction. The corresponding calibration factor is therefore

$$\Delta C_p = \frac{5.0}{618} \approx 8.1 \times 10^{-3}\ C_p/\text{pixel}. \tag{5}$$

Repeated picking of points on the same plotted curve typically exhibits a vertical scatter of 3–4 pixels due to line thickness, anti-aliasing, and cursor placement. Multiplying this scatter by the calibrated factor yields 0.03. The error bars in Figure 11 therefore represent the digitization uncertainty of the extracted curves. Alignment verified by checking that (i) the trailing-edge $C_p$levels from suction and pressure sides coincide within the digitization band and (ii) the integrated loads are consistent with the corresponding NREL polar at the same angle.

Experimental uncertainties were kept exactly as published by NREL. When the source provided uncertainty bounds, those values were used directly in figures or tables without re-processing. The digitization uncertainty relates only to converting the plotted curves into numerical data and was quantified independently as explained above.

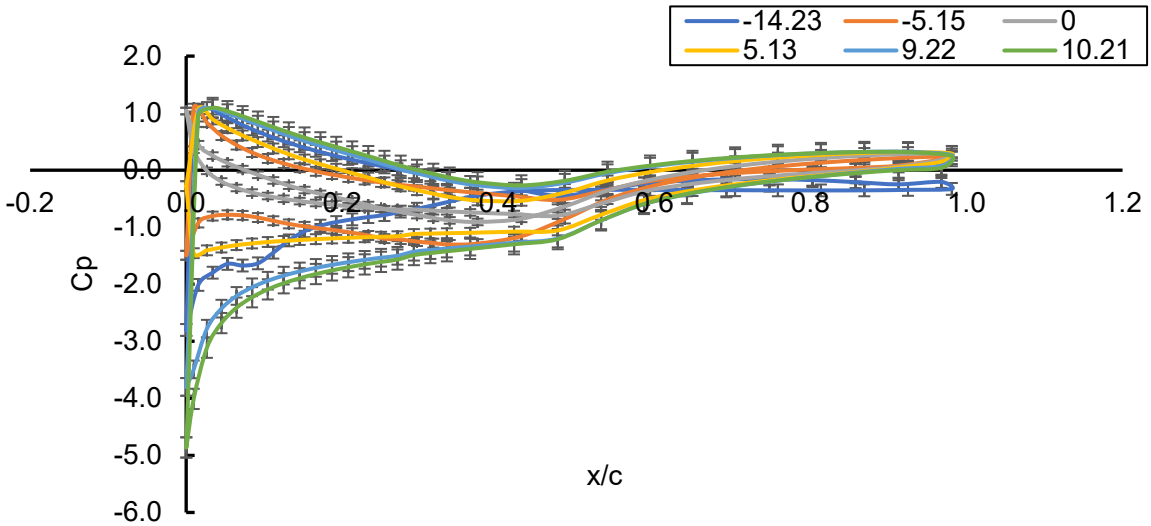

Fig. 11 *Pressure coefficient Cp digitization error and uncertainty*

Int. Journal of Integrated Engineering Vol. 17 No. 8 (2025) p. 341-361

The experimental data used here is the NREL S809 two-dimensional wind-tunnel data. The work did not re-apply any additional tunnel corrections. In the CFD, the airfoil was modeled as an isolated 2-D section with large far-field boundaries (domain radius 7.5 c; total diameter 15 c), and a no-slip wall on the airfoil; therefore, support and wall effects present in the tunnel are intentionally absent from the simulation. Any residual tunnel interference that remains in the experimental data is thus expected to appear as a small, systematic bias in comparisons which are most noticeably near stall. For Reynolds number sensitivity, the experiments and simulations were matched at 2 million as in the NREL experimental work.

3. Results

This subchapter presents a comprehensive analysis of the aerodynamic performance of the S809 airfoil based on a series of Computational Fluid Dynamics (CFD) simulations. The results are structured around two core investigations: the impact of angle of attack (AoA) variations and the comparative performance of different turbulence models. Initially, a parametric sweep across a wide range of AoA values was conducted to determine the optimum operating condition in terms of lift, drag, and pressure distribution. This enabled the identification of stall onset, maximum lift-to-drag ratio, and performance trends under pre-stall regime. Subsequently, a turbulence model sensitivity study was carried out to evaluate the predictive capabilities of widely used RANS-based models including k-ω, and SST k-ω models under the selected optimum AoA. Each model's performance was assessed based on pressure coefficient distribution, force coefficients, and agreement with experimental benchmarks. Together, these results provide a validated and insightful understanding of the aerodynamic characteristics of the S809 airfoil, while also emphasizing the influence of turbulence modelling on flow accuracy and stability.

3.1 Turbulence Model Comparative Study

Two turbulence models Standard k-ω, and k-ω SST were used to simulate the aerodynamic performance of the S809 airfoil. For each model, the lift coefficient (CL), drag coefficient (CD), and the lift-to-drag ratio (CL/CD) were calculated over a range of angles of attack. The results showed variation in the values of CL and CD between the models at different angles where the k-ω and k-ω SST models presented different magnitudes and distributions for both CL and CD across the AoA range. All data were obtained under the same flow conditions and mesh settings to ensure consistency during the turbulence model evaluation

3.1.1 K-ω SST

The k-ω SST turbulence model showed a mostly accurate trend in simulating the S809 airfoil's aerodynamic coefficients at different angles of attack. The model consistently overpredicted the lift coefficient (Cl) when compared to experimental benchmarks. Figure 12, for example, shows how the S809 flowfield changes under k–ω SST across six incidences and shows a clear stall pathway. At α=−14.23° (a), the upper surface (the pressure side at negative α) separates at the nose. A thick separated shear layer moves to the trailing edge without reattachment, leaving a wide, deep wake. The lower surface acceleration is weak and short, with an imprint of reversed loading that causes large pressure drag and strongly negative lift. At 5.13° (b), the irregularity is lessened: separation moves downstream into a compact behind little, the lower surface speeds up and recovers smoothly, and the wake narrows, which is in line with a smaller amount of negative lift and less pressure loss. At 0° (c), the shapes are almost symmetric. This means that the flow is attached and there is about 0 lift. This panel sets the clean baseline for positive incidence. At 5.14° (d), the suction side has a sharp leading-edge acceleration followed by a long-attached region to about 0.7–0.8c. Any separation is limited to a short trailing-edge. The wake stays thin, marking the pre-stall optimum where lift is created efficiently with little pressure-drag penalty. The adverse pressure gradient moves forward as the angle increases to 9.22° (e). The suction-side boundary layer gets thicker by mid-chord, a mid-chord separation levels forms, the wake gets wider and deeper, and the flow starts to stall, with drag rising quickly even as lift is near its peak. The separated area covers most of the suction surface at 10.21° (f), and there is no credible reattachment before the trailing edge. The wake becomes wide and very weak, which is typical of post-stall with saturated (or declining) lift and separated-flow pressure drag that is dominant.

Taken together, the panels isolate the aerodynamic controls that set the S809's usable operating margin. The stagnation-point shift, leading-edge acceleration, and progressive upstream migration of separation determine suction-side loading, while the wake thickness and velocity deficit quantify the pressure-drag penalty. Efficient operation corresponds to the regime in (d), where attached suction is sustained over most of the chord; (e) visualizes the tipping point where separation moves forward and the wake rapidly thickens; and (f) demonstrates the loss-dominated state once reattachment collapses.

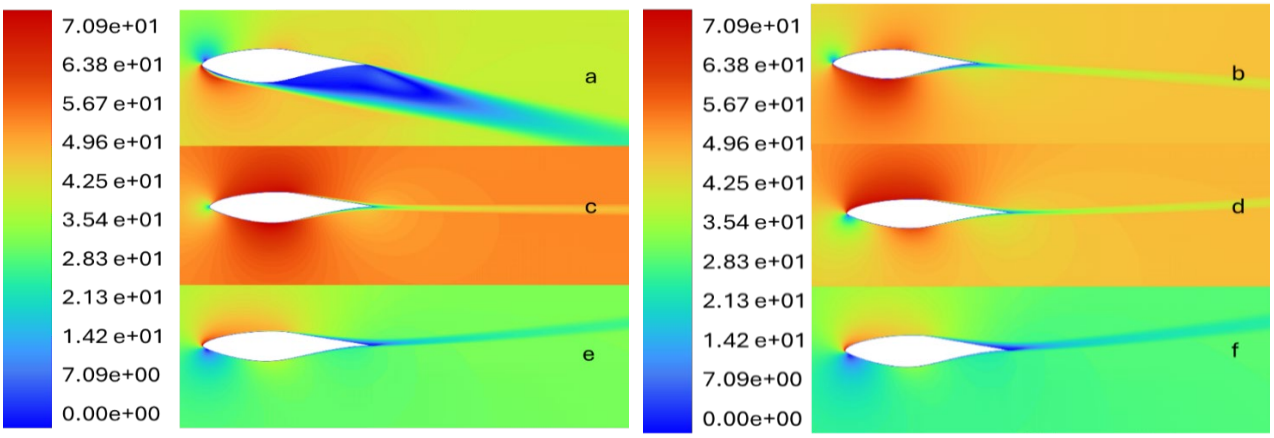

Fig. 12 *S809 airfoil, k-ω SST turbulence model for (a) -14.23AoA, (b) -5.13 AoA, (c) 0 AoA, (d) 5.14 AoA, (e) 9.22 AoA, and (f) 10.21 AoA*

Figure 13 (a) illustrates a continuous, nearly linear increase in lift from negative to mild positive incidence, with the k–ω SST solution accurately following the actual slope within the attached-flow region and deviating only as flow separation becomes significant. Between α = −14.23° and −5.14°, the SST curve is positioned marginally above the experimental trend, which exhibited immediate upper-surface separation at −14.23° and a substantial wake. However, the model retains a more coherent suction on the reversed lower surface, resulting in a less negative CL than observed. Between α = 0° and 9.22°, both curves converge on the same gradient, aligning with the velocity maps at 5.14° and 9.22°, where the suction side predominantly remains attached and only a compact mid-chord levels develops; in this region, the integrated lift is determined by the forward suction level effectively represented by SST. At 10.21°, the numerical lift coefficient remains marginally elevated compared to the experimental stall, which is less severe.

The drag trends in Figure 13 (b) are governed by the wake development illustrated in the contours. At −14.23°, the experiment indicates a significant and continuous drag coefficient (CD). As the incidence approaches −5.14° and 0°, both curves converge towards a shallow minimum, consistent with computational fluid dynamics and experimental experiments. Between 5.13° and 9.22°, the measured drag coefficient increases as the mid-chord levels enlarges, whereas the rise in wake is less pronounced, at 10.21°. The experiment maintains a higher drag level due to complete suction-side separation; however, the wake still exhibits partial attachment and a reduced wake, resulting in an underestimation of the pressure-drag component. The coefficient plots and velocity fields convey a coherent narrative. (i) The lift coefficient (CL) agreement is robust while the boundary layer remains attached, exhibiting excess computed lift as separation progresses; (ii) The drag coefficient (CD) is consistently low when the wake is expected to be thick, indicating the model's propensity to postpone or mitigate separation.

Figure 14 compares C_p for x/c curves from the simulation with the NREL measurements at six angles of attack: −14.23°, −5.14°, 0°, 5.13°, 9.22°, and 10.21°. For both negative angles, the two curves nearly coincide along most of the chord, with small differences very close to the leading edge and near $x/c \approx 1$. At 0° and 5.13°, the simulated trend follows the measured one across the chord; differences are modest and are most visible between $x/c \approx 0.2$and 0.6. At 9.22° and 10.21°, the separation between simulated and measured curves is larger, especially over $x/c \approx 0.1$–0.6, while values near the trailing edge remain similar. Overall, the plots show good agreement at low and negative angles, with deviations increasing progressively as the angle of attack rises.

Int. Journal of Integrated Engineering Vol. 17 No. 8 (2025) p. 341-361

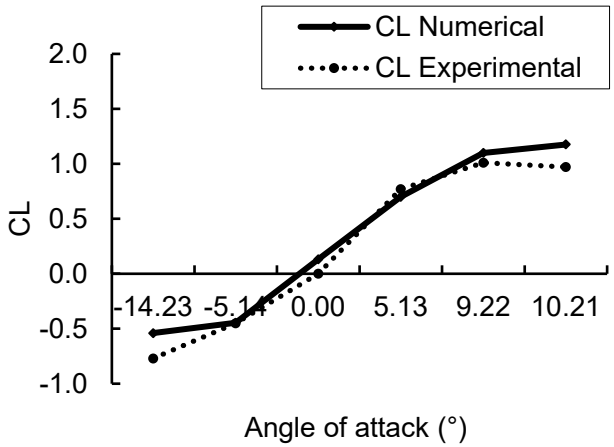

(a) *CL results for k-w SST turbulence model*

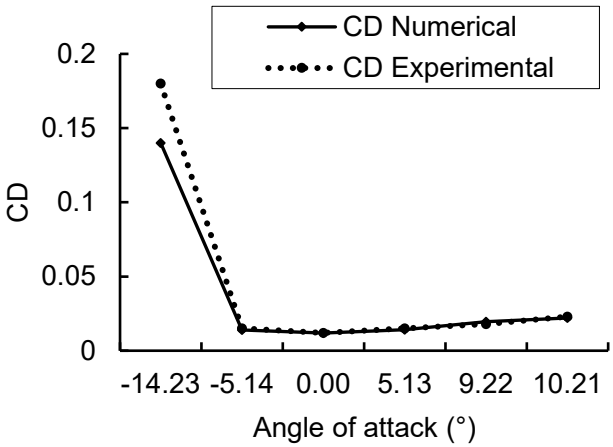

(b) *CD results for k-w SST turbulence model*

Fig. 13 *S809 airfoil, k-ω SST turbulence model (a) CL, (b) CD*

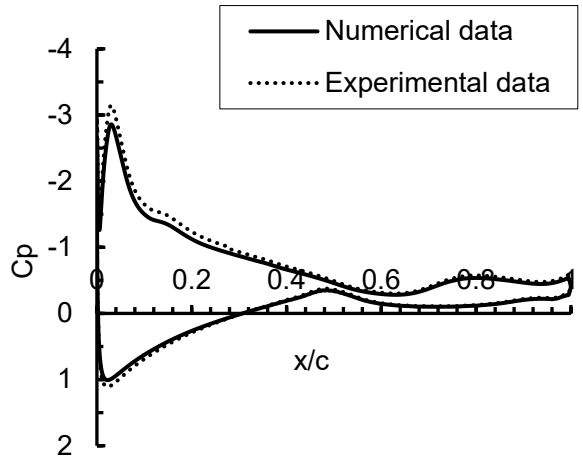

(a) *(α = -14.23°)*

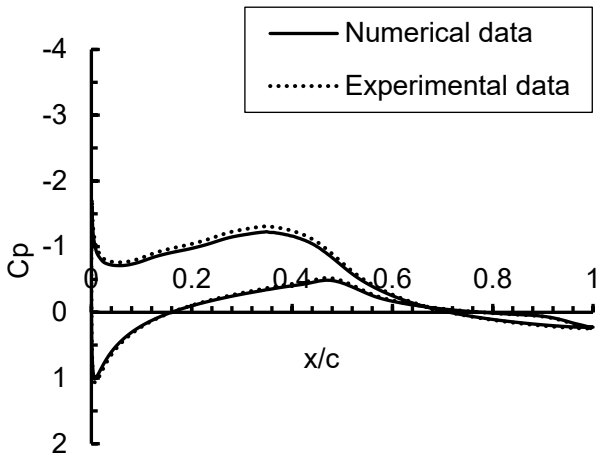

(b) *(α = -5.14°)*

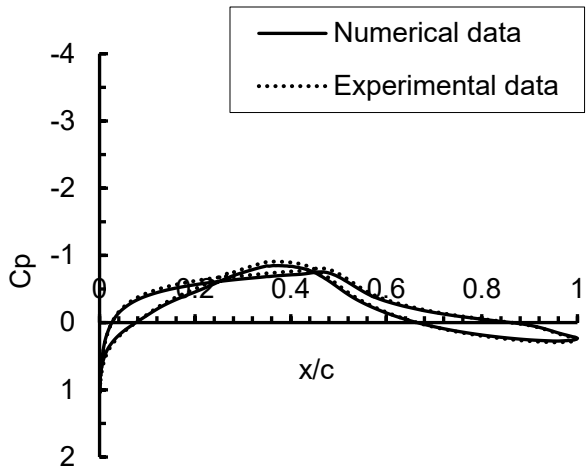

(c) *(α = 0°)*

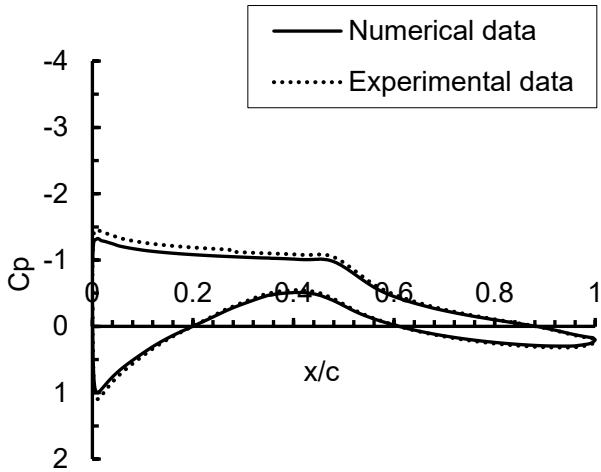

(d) *(α = 5.13°)*

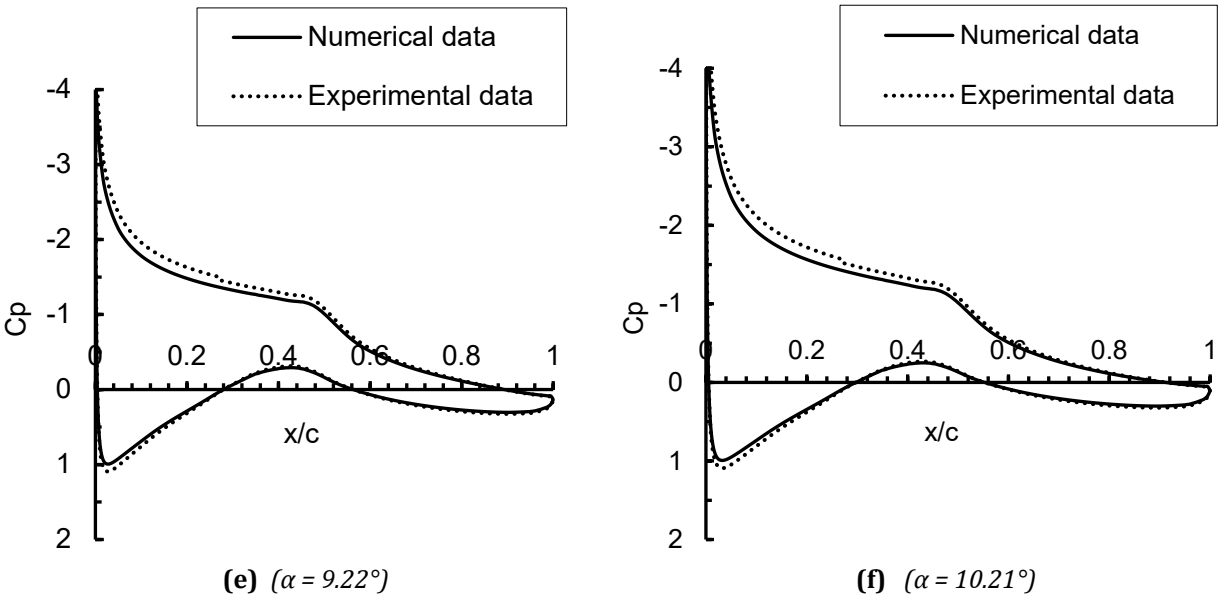

Fig. 14 *S809 airfoil, k-ω SST turbulence model Cp values comparison between Experimental and Numerical works for (a) -14.23AoA, (b) -5.13 AoA, (c) 0 AoA, (d) 5.14 AoA, (e) 9.22 AoA, and (f) 10.21 AoA*

Figure 15 summarizes the aerodynamic performance of the S809 into one measure, CL/CD, across incidence. When the AoA is negative, the ratio is also negative, with a clear dip near −5.14°. This is because the loading is reversed and there is a lot of pressure drag from the separated upper surface seen in the contours. The numerical curve is less negative than the experimental one because SST keeps too much coherence on the reversed suction side, which results in a less negative CL and a slightly underpredicted CD. The ratio rises quickly from 0° to 5.13° as the suction-side attachment forms and the wake narrows. In this range, both curves have almost the same slope, which is in line with the Cp panels where the boundary layer stays mostly attached and drag is mostly caused by skin friction. The highest efficiency happens at about 9.22°, which is a few points higher than the experimental direct effect of the model's overprediction of CL and underestimation of pressure drag when the mid-chord separation levels first appear.

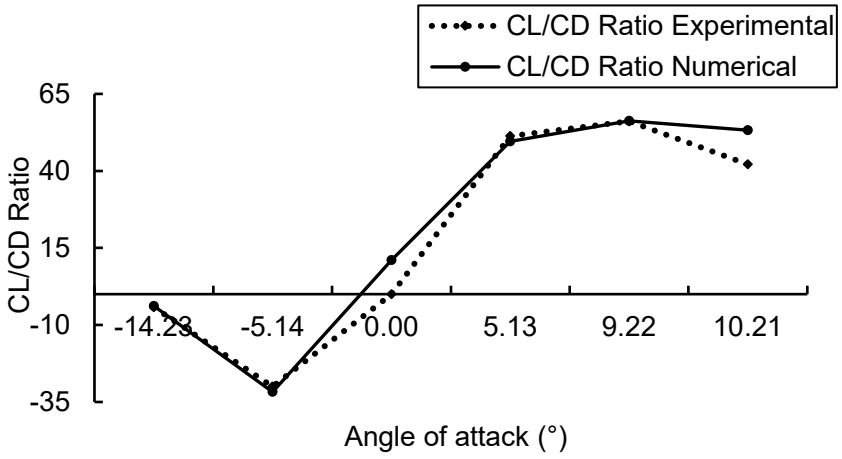

Fig. 15 *S809 airfoil, k-ω SST turbulence model CL/CD ratio comparison between Experimental and CFD Numerical works*

At six angles of attack, Table 7 compares the NREL data to k-ω SST. At −14.23°, both coefficients are lower than what was measured (CL −0.562 vs −0.77; CD 0.134 vs 0.180). At −5.14°, lift and drag are equal (CL −0.444 vs −0.45; CD 0.020 vs 0.015). The model shows a small amount of positive lift and a little bit more drag at 0.00° (CL 0.141 vs. 0.00; CD 0.013 vs. 0.012). At 5.13°, lift is a little low and drag is the same (CL 0.718 vs 0.77; CD 0.015 vs 0.015). At 9.22°, both lift and drag are higher than the data (CL 1.136 vs 1.01; CD 0.021 vs 0.018). At 10.21°, lift stays high and drag is the same as the measurement (CL 1.226 vs 0.97; CD 0.023 vs 0.023). Overall, agreement is

Int. Journal of Integrated Engineering Vol. 17 No. 8 (2025) p. 341-361

strong near −5.14° and 5.13°, weak at −14.23°, slightly biassed at 0.00°, and strong at 9.22° and 10.21° with drag also strong at 9.22°.

Table 7 *S809 CFD using k-w SST turbulence model performance in comparison with NREL experimental work*

	NREL Experimental		CFD Numerical			
AoA (°)	CL (EXP)	CD (EXP)	CD (CFD)	CL (CFD)	CL Error %	CD Error %
-14.23	-0.77	0.180	0.140	-0.858	11.39	22.22
-5.14	-0.45	0.015	0.014	-0.445	1.12	6.53
0.00	0.14	0.012	0.012	0.132	5.98	0.91
5.13	0.77	0.015	0.014	0.699	9.20	5.99
9.22	1.01	0.018	0.020	1.099	8.79	-8.53
10.21	0.97	0.023	0.022	1.176	21.19	3.98

3.1.2 K-ω Standard

The k–ω Standard model in Figure 16 shows a clear pattern across the angles of attack. It is different from SST in a few ways. At negative angles, the low-speed area on the pressure side is shorter and thinner than in SST. This means that less momentum is lost before the trailing edge, and the wake becomes narrow earlier. The front part is clean at about 0°, both sides stay attached across the chord, and the wake is thin with no clear area where the trailing edge separates. At moderate positive angles, the acceleration at the front is less strong than in SST. The attached flow goes further downstream, there is only a small, separated area near the trailing edge, and the wake stays narrow.

The behavior can be seen in panels e and f, which are close to the stall. At 9.22°, the flow stays attached over the front half of the chord, the mid-chord shows only a mild low-speed region, and the wake gets thicker, but it does so slowly. By 10.21°, a separate region forms near the back and stays fairly compact. The low-speed area downstream gets bigger, but not as big as it would be if the flow were fully separated on the upper side. When you look at all of these fields together, they show that the k–ω Standard model tends to delay separation and slow down the growth of the wake. This means that the airfoil has slightly low drag and slightly high lift as it gets closer to stalling, but it stays smooth and steady in the pre-stall range.

The k–ω Standard model depicted in Figure 17 consistently yields a higher CL than the experimental results across the six instances. The numbers at −14.23° and −5.14° are less negative than the measurements, which means that reverse loading is weaker. The calculation already gives a positive CL at 0°, but the experiment is still close to zero. The numerical and experimental slopes are similar from 5.13° to 9.22°, but the numerical curve stays above the data. The gap is still there at 10.21°, and the model shows the biggest positive bias in CL among the positive-AoA points. At all angles, the calculated CD is lower than the experimental value. The difference is biggest at −14.23°, where the measurement shows a high loss level but the model shows a lower drag. Both curves reach their lowest point near −5.14°–5.13°, but the numbers are still lower than the data. The experimental drag goes up from 9.22° to 10.21°, but the numerical rise is weaker, which keeps the computed CD below the measurement at the two highest angles.

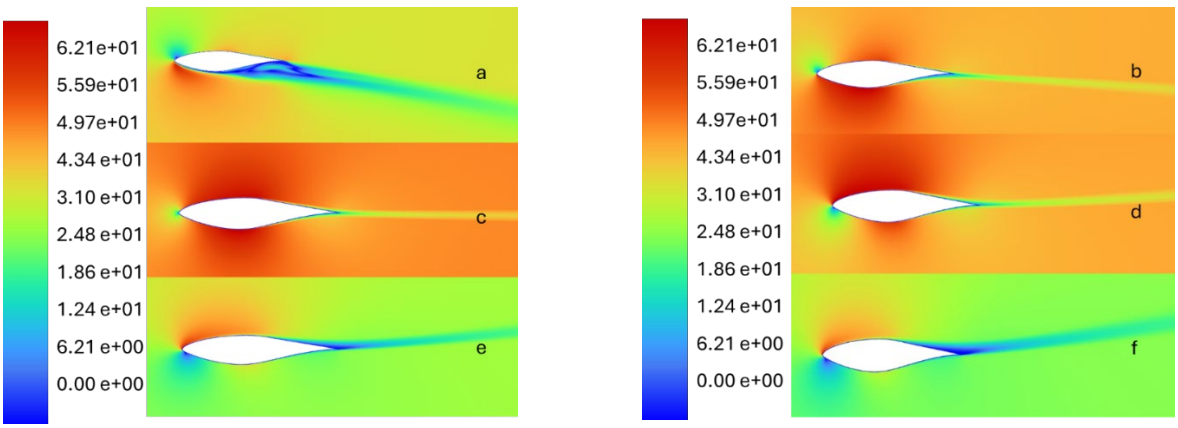

Fig. 16 *S809 airfoil, k-ω standard turbulence model for (a) -14.23AoA; (b) -5.13 AoA; (c) 0 AoA; (d) 5.14 AoA; (e) 9.22 AoA; and (f) 10.21 AoA*

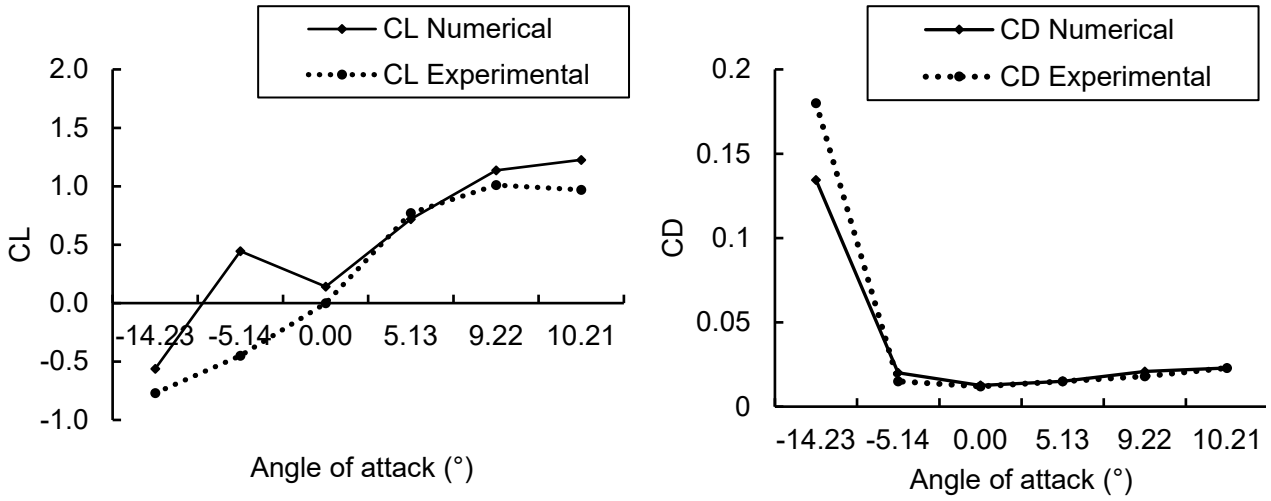

Fig. 17 *S809 airfoil, k-ω standard turbulence model (a) CL; (b) CD*

In the six Cp panels shown in Figure 18 for the k–ω Standard model, the main difference is that the suction is weaker and the recovery is smoother than in the experiment at all angles of incidence. This difference gets bigger as the angle of incidence increases. In the two negative AoA cases, the experimental lower-surface peak is deeper and the upper-surface recovery is thicker. The numerical upper branch is closer to zero over the mid-aft chord, which means the pressure difference is smaller in magnitude. This explains the less-negative CL and lower CD seen in the coefficients. The two datasets are close at 0°, but the computation already shows a slightly higher suction level and an earlier return of the lower branch to Cp≈0. The crossover stays close to x/c≈0.55x, which is consistent with a near-zero-lift condition. At 5.13°, the experiment creates a sharper LE suction and a more pronounced crest around x/c ≈0.35 to 0.45. The numerical curve flattens that crest and spreads it downstream, keeping the upper branch too high (less negative) and the lower branch too low (more positive) over mid-chord. This means that lift is maintained by a broader but milder loading instead of a focused peak.

At 9.22° and 10.21°, the differences are most clear. In the experiment, the upper branch shows a sudden rise in Cp starting around x/c ≈0.45 to 0.6. This means that there is a mid-chord separation levels and an early loss of suction. At the same time, the lower branch trends upward towards zero. The k–ω Standard prediction shows a more negative upper branch before the rise and a gentler recovery through the crossover. This gives a higher CL and lower pressure drag than what was measured. At 10.21°, the experimental upper branch is mostly separated (long, shallow level with late recovery). The numerical curve, on the other hand, still has some attachment and a steeper pressure recovery from mid-chord to the trailing edge. The lower branch stays slightly below the data. So, the mechanism is the same across the panels: the model delays the start of separation (the upper branch stays more negative up to x/c0.5) and doesn't develop the aft deficit enough (a smoother rise and thinner wake are implied), which together explain the coefficient-level pattern that overpredicts lift and underpredicts drag near and beyond stall, with reasonable agreement in the attached regime.

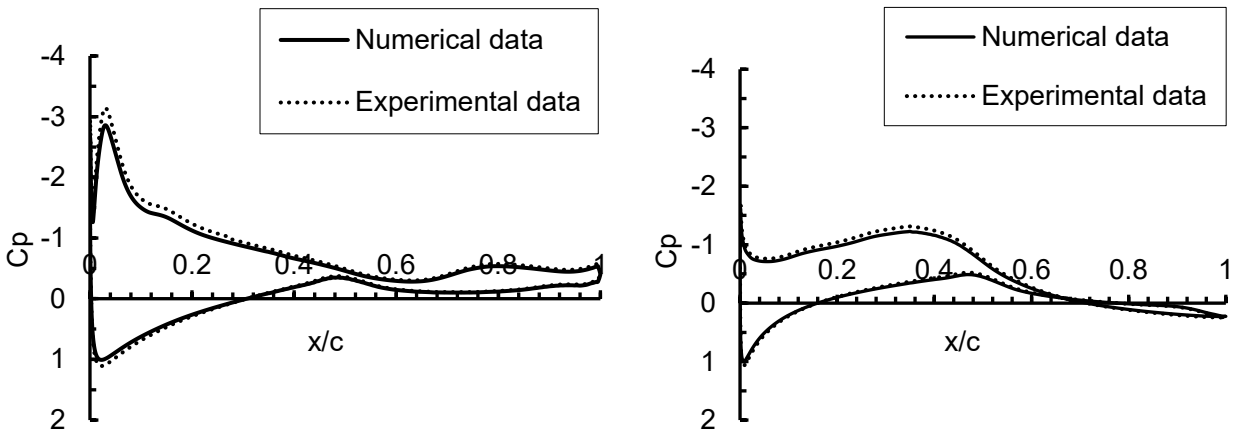

(a) *(α = -14.23°)* **(b)** *(α = -5.14°)*

Int. Journal of Integrated Engineering Vol. 17 No. 8 (2025) p. 341-361

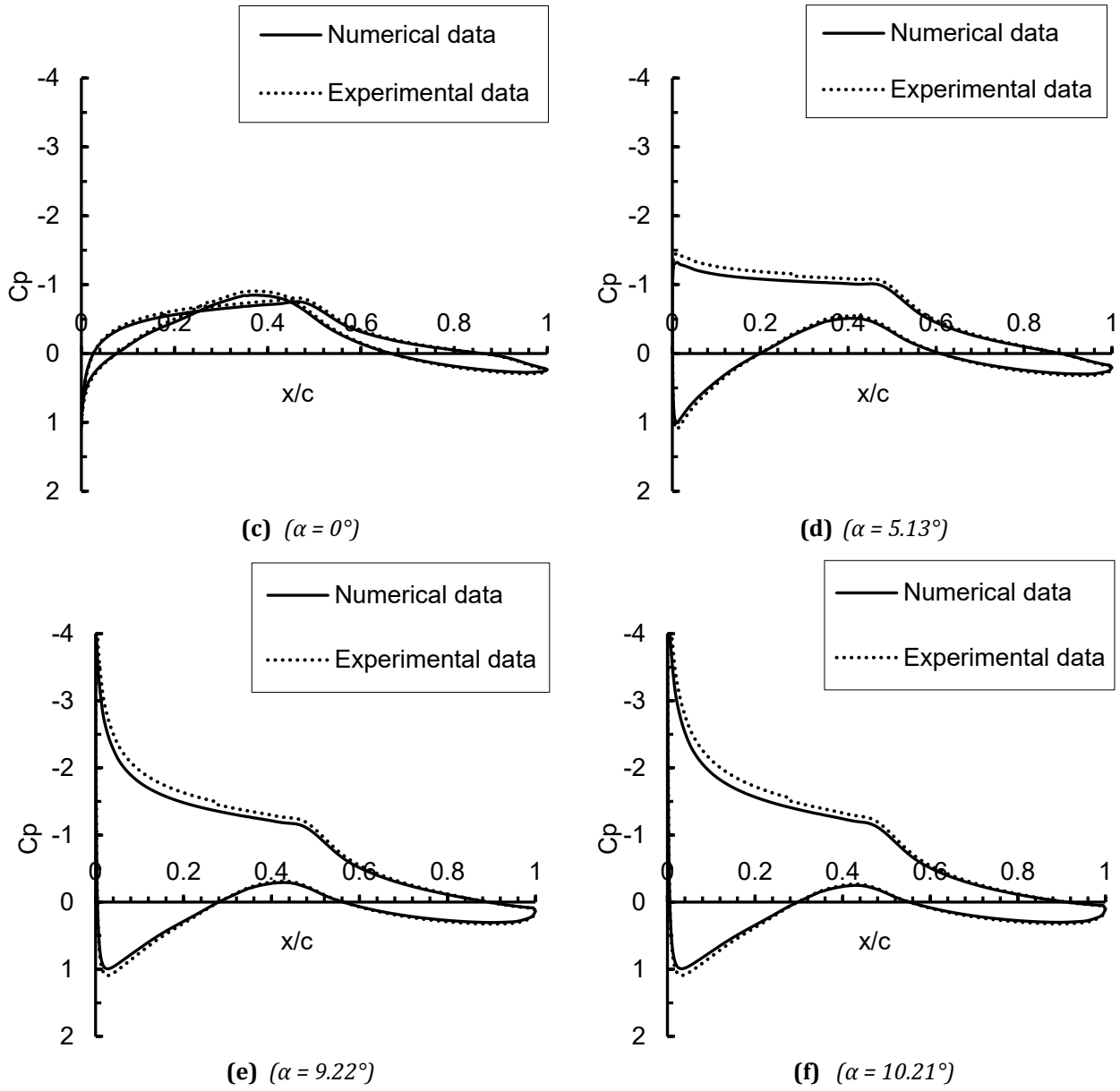

Fig. 18 *S809 airfoil, k-ω Standard turbulence model Cp values comparison between Experimental and Numerical works for (a) -14.23AoA, (b) -5.13 AoA, (c) 0 AoA, (d) 5.14 AoA, (e) 9.22 AoA, and (f) 10.21 AoA*

Figure 19 shows that at the two negative incidences (−14.23°, −5.14°), the numerical ratio is less negative than the experimental ratio. This is because the k–ω Standard solution makes the reverse lift weaker and the drag lower than the measurements, which makes CL/CD smaller. The numerical curve crosses into positive CL/CD near 0°, but the experimental point stays close to zero. The computation gives a small positive CL and a low CD, which raises the ratio above the data at the zero-lift condition. From 5.13° to 9.22°, both curves rise quickly and show where the efficiency levels. The numerical ratio at 5.13° is close to the experiment's ratio, but it is higher at 9.22°. The k–ω Standard model has a slightly stronger suction load and a slimmer wake, which makes CL higher and CD lower, pushing CL/CD up. The experimental ratio drops at 10.21°, which is in line with the general separation of the suction side. The numerical ratio drops less and stays above the experiment because the model keeps partial attachment and underpredicts pressure drag. The plot shows that the k–ω Standard model consistently overpredicts CL/CD at and above the efficiency peak. The biggest differences happen when the airfoil starts to stall.

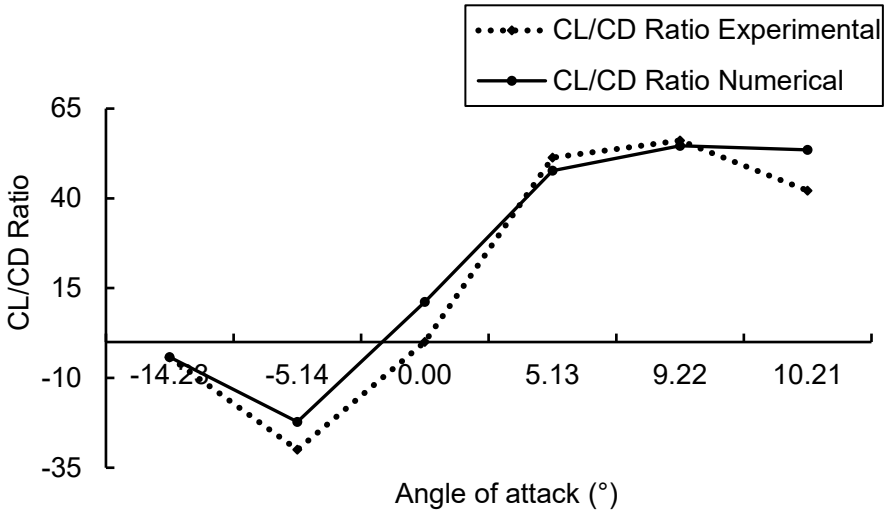

Fig. 19 *S809 airfoil, k-ω standard turbulence model cl/cd ratio comparison between experimental and cfd numerical works*

Table 8 shows how lift and drag change at six different angles of attack. The model underpredicts lift (−0.54 vs. −0.77; ΔCL = 0.23, −29.94%) and drag (0.140 vs. 0.180; ΔCD = −0.040, −22.22%) at −14.23°. The two coefficients are very close at −5.14° (CL = −0.44 vs. −0.45; −1.12%; CD = 0.014 vs. 0.015; −6.53%). The experiment shows CL = 0.00 at 0.00°, so there is no percentage error. The model shows CL = 0.13 and CD = 0.012, which is the same as the experimental drag (0.012, −0.91%). Lift errors are still moderate in the pre-stall range (0.70 vs. 0.77, −9.20%; 1.10 vs. 1.01, +8.79%), and drag errors are within ±9% (0.014 vs. 0.015, −5.99%; 0.020 vs. 0.018, +8.53%). The model overestimates lift at 10.21° (1.18 vs. 0.97; ΔCL = 0.21, +21.19%), but drag stays close to the measurement (0.022 vs. 0.023; −3.98%).

Table 8 *S809 CFD using k-w Standard turbulence model performance in comparison with NREL experimental work*

	NREL Experimental		CFD Numerical			
AoA (°)	CL (EXP)	CD (EXP)	CD (CFD)	CL (CFD)	CL Error %	CD Error %
-14.23	-0.77	0.180	0.134	0.562	27.06	25.30
-5.14	-0.45	0.015	0.018	0.427	4.97	-24.49
0.00	0.14	0.012	0.013	0.141	-0.53	-4.68
5.13	0.77	0.015	0.015	0.718	6.73	-0.42
9.22	1.01	0.018	0.021	1.136	-12.47	-15.49
10.21	0.97	0.023	0.023	1.226	-26.42	0.39

4. Conclusion

This study examined the S809 airfoil at six angles of attack: −14.23°, −5.15°, 0°, 5.13°, 9.22°, and 10.21°. It also looked at how coefficient trends were related to surface pressure and velocity fields. The k–ω SST and k–ω Standard both showed the pre-stall range between 5.13° and 10.21°, with attached flow on the upper surface, a thin wake, and a lift-curve slope that matched the measurements. In the wind-tunnel data, stall onset looked like higher pressure on the upper surface near mid-chord and a quick thickening of the wake. The SST model captured this sequence but with less intensity, and the Standard model moved it to a higher angle. As a result, both models overestimated the lift-to-drag ratio at 9.22° and 10.21°. This was because the lift was too high and the pressure drag was too low because the low-pressure areas lasted too long and the wake didn't grow enough. At negative angles of −14.23° and −5.15°, the tunnel showed immediate separation on the pressure side with large losses. However, both models, especially Standard, predicted a thinner separated region, a smaller negative lift, and less drag. At nominal 0°, the numerical solutions yielded a slight positive lift, while the drag corresponded with the measurements, suggesting a residual circulation bias rather than a friction-model discrepancy.

Three options made the results more believable. First, every trend in the coefficients was connected to certain characteristics in the pressure and velocity fields. This means that integrals alone were not used to judge agreement. Second, the experimental surface pressure data were used directly through careful digitisation and

Int. Journal of Integrated Engineering Vol. 17 No. 8 (2025) p. 341-361

calibrated axis mapping. This meant that validation included both the distribution of loading and the total values. Third, a side-by-side comparison of the two k–ω models made their roles clearer: SST works well when the flow stays attached and reproduces the observed stall sequence, but it needs to be fixed near separation. The Standard model gives smooth, conservative drag when the flow is attached, but it becomes too optimistic in lift as separation grows. For design and control, the S809 should be set to work between 5.13° and 9.22°, and the operating set-point should stay below the experimental peak, which is around 9.22°, to avoid the quick drop in efficiency that follows. When working close to a stall, SST should be used with either transition control or light separation calibration based on surface pressure or wake profiles. The uncertainty bands should show the observed biases: lift should be about 10–20% higher and drag should be about 5–10% lower at and above 10.21°. Three things are most likely to lead to more improvement: making the transition clearer, getting a better resolution near the leading edge to find the leading-edge pressure minimum, and tuning the pressure-drag based on measured wake data. These steps close the gap between the current performance and the wind-tunnel benchmarks while keeping the strong performance before the stall that was shown here.

4.1 Recommendation and Future Work

The present analysis establishes a reliable baseline for the S809 in attached and near-stall conditions with k-ω SST and k-ω Standard, but three areas should be prioritized to harden the conclusions and extend applicability. First, refine transition treatment and leading-edge resolution. Prescribe or predict transition and perform a targeted grid study that resolves the nose suction spike, maintains y-plus near unity, and quantifies the impact of near-wall numeric on the growth and migration of separation. Second, strengthen validation at the loading and wake levels. Enhance the current Cp digitization with pressure-tap reconstructions at matched x over c stations and pair them with wake momentum thickness or hot-wire or PIV velocity deficits, so pressure drag and separation length are constrained independently of the lift curve. Third, formalize model calibration and uncertainty. Use coefficient and Cp residuals to build simple correction laws for suction level height and aft recovery, and report uncertainty bands that carry through to lift-to-drag and recommended operating angles.

To extend the physics envelope, the next phase of this work will analyze post-stall angles of attack using transient URANS such as the shown figure below Figure 20. This continuation will resolve unsteady separation, vortex shedding, and hysteresis, quantify cycle-averaged loads and load spectra, and test whether k-ω SST with transition control is sufficient or whether a hybrid RANS–LES treatment is required in deep stall. Additional studies should examine sensitivity to Reynolds' number and surface condition, including leading-edge roughness representative of insect contamination, and verify two-dimensional assumptions with a finite-span check to exclude stall-cell bias. Finally, the methodology will be packaged for design use: Cp-based calibration terms tied to measurable wake metrics, a documented grid and transition recipe for reproducibility, and a recommended operating window that includes a margin below the experimental efficiency peak to account for the observed model biases near stall.

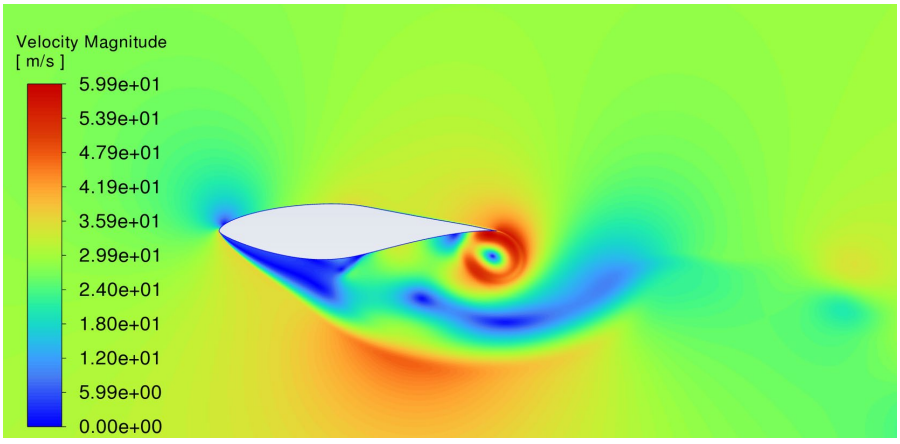

Fig. 20 *S809 airfoil velocity contour for AoA -17.17 using URANS transient set up*

Acknowledgement

Communication and the conduct of this research are made possible through the Faculty of Mechanical and Manufacturing Engineering at Universiti Tun Hussein Onn Malaysia (UTHM) and the National Renewable Energy Laboratory (NREL) data.

Conflict of Interest

Authors declare that there is no conflict of interests regarding the publication of the paper.

Author Contribution

The authors confirm contribution to the paper as follows: ***Data curation, Formal analysis, Investigation, Conceptualization, Methodology, Software, Validation, Visualization, Writing - original draft, Writing - review & editing:*** *Abobakr Al-ttowi;* ***supervision, Conceptualization, Project administration, Methodology, Writing - review & editing, Formal analysis, Resources, Data curation, Visualization:*** *Akmal Nizam Mohammed. All authors reviewed the results and approved the final version of the manuscript.*

References

[1] M. T. Akram and M. H. Kim, "Aerodynamic shape optimization of nrel s809 airfoil for wind turbine blades using reynolds-averaged navier stokes model—part ii," Applied Sciences (Switzerland), vol. 11, no. 5, pp. 1–26, Mar. 2021, doi: 10.3390/app11052211.

[2] T. Dhert, T. Ashuri, and J. R. R. A. Martins, "Aerodynamic shape optimization of wind turbine blades using a Reynolds-averaged Navier–Stokes model and an adjoint method," Wind Energy, vol. 20, no. 5, pp. 909–926, May 2017, doi: 10.1002/we.2070.

[3] S. Aziz et al., "Computational Fluid Dynamics and Experimental Analysis of a Wind Turbine Blade's Frontal Section with and without Arrays of Dimpled Structures," Energies (Basel), vol. 15, no. 19, Oct. 2022, doi: 10.3390/en15197108.

[4] A. Al-Ttowi, A. N. Mohammed, S. Al-Alimi, W. Zhou, Y. Saif, and I. F. Ismail, "Computational Fluid Dynamics (CFD) Investigation of NREL Phase VI Wind Turbine Performance Using Various Turbulence Models," Processes, vol. 12, no. 9, Sep. 2024, doi: 10.3390/pr12091994.

[5] O. Guerri, K. Bouhadef, and A. Harhad, "Turbulent flow simulation of the NREL S809 airfoil," Wind Engineering, vol. 30, no. 4, pp. 287–302, May 2006, doi: 10.1260/030952406779295471.

[6] J. N. Sørensen and W. Z. Shen, "Numerical modeling of wind turbine wakes," Journal of Fluids Engineering, Transactions of the ASME, vol. 124, no. 2, pp. 393–399, 2002, doi: 10.1115/1.1471361.

[7] C. Traylor, M. DiPaola, D. J. Willis, and M. Inalpolat, "A computational investigation of airfoil aeroacoustics for structural health monitoring of wind turbine blades," Wind Energy, vol. 23, no. 3, pp. 795–809, Mar. 2020, doi: 10.1002/we.2459.

[8] W. Zhong, H. Tang, T. Wang, and C. Zhu, "Accurate RANS simulation ofwind turbine stall by turbulence coefficient calibration," Applied Sciences (Switzerland), vol. 8, no. 9, Aug. 2018, doi: 10.3390/app8091444.

[9] F. Bertagnolio, F. Rasmussen, N. N. Sørensen, J. Johansen, and H. A. Madsen, "A stochastic model for the simulation of wind turbine blades in static stall," Wind Energy, vol. 13, no. 4, pp. 323–338, 2010, doi: 10.1002/we.342.

[10] R. Gutierrez, R. Zamponi, D. Ragni, E. Llorente, and P. Aranguren, "On the extension of k–ω–SST corrections to predict flow separation on thick airfoils with leading-edge roughness," Wind Energy, vol. 26, no. 7, pp. 650–667, Jul. 2023, doi: 10.1002/we.2822.

[11] O. Guerri, K. Bouhadef, and A. Harhad, "Turbulent flow simulation of the NREL S809 airfoil," Wind Engineering, vol. 30, no. 4, pp. 287–302, May 2006, doi: 10.1260/030952406779295471.

[12] G. Dejene, V. R. Ancha, and A. Bekele, "NREL Phase VI wind turbine blade tip with S809 airfoil profile winglet design and performance analysis using computational fluid dynamics," Cogent Eng, vol. 11, no. 1, 2024, doi: 10.1080/23311916.2023.2293562.

[13] T.-H. Shih, W. W. Liou, A. Shabbir, Z. Yang, and J. Zhu, "A New k-ε Eddy Viscosity Model for High Reynolds Number Turbulent Flows," 1995.

[14] W. Zhong, H. Tang, T. Wang, and C. Zhu, "Accurate RANS simulation ofwind turbine stall by turbulence coefficient calibration," Applied Sciences (Switzerland), vol. 8, no. 9, Aug. 2018, doi: 10.3390/app8091444.

[15] S. Younoussi and A. Ettaouil, "Calibration method of the k-ω SST turbulence model for wind turbine performance prediction near stall condition," Heliyon, vol. 10, no. 1, Jan. 2024, doi: 10.1016/j.heliyon.2024.e24048.

[16] S. Younoussi and A. Ettaouil, "Calibration method of the k-ω SST turbulence model for wind turbine performance prediction near stall condition," Heliyon, vol. 10, no. 1, Jan. 2024, doi: 10.1016/j.heliyon.2024.e24048.

Int. Journal of Integrated Engineering Vol. 17 No. 8 (2025) p. 341-361

[17] S. R. Allmaras, “AlAA-92-G439 A One-Equatlon Turbulence Model for Aerodynamic Flows.”

[18] T. J. Craft, B. E. Launder, and K. Suga, “Development and application of a cubic eddy-viscosity model of turbulence,” 1996.

[19] P. R. Spalart, S. Deck, M. L. Shur, K. D. Squires, M. K. Strelets, and A. Travin, “A new version of detached-eddy simulation, resistant to ambiguous grid densities,” Theor Comput Fluid Dyn, vol. 20, no. 3, pp. 181–195, Jul. 2006, doi: 10.1007/s00162-006-0015-0.

[20] I. Solís-Gallego, K. M. A. Díaz, J. M. F. Oro, and S. Velarde-Suárez, “Wall-resolved LES modeling of aWind turbine airfoil at different angles of attack,” J Mar Sci Eng, vol. 8, no. 3, Mar. 2020, doi: 10.3390/jmse8030212.

[21] Fluent Thoery Guide, “Ansys Fluent Theory Guide,” ANSYS Inc., USA, vol. 15317, no. November, pp. 724–746, 2013, [Online]. Available: http://scholar.google.com/scholar?hl=en&btnG=Search&q=intitle:ANSYS+FLUENT+Theory+Guide#0

[22] “NREL’s S809 Airfoil (s809-nr).”

[23] D. M. Somers, “Design and Experimental Results for the S809 Airfoil,” 1997.